

A Three-Dimensional Model of the Resin Film Infusion Process

A.C. LOOS,* D. RATTAZZI AND R.C. BATRA

Engineering Science and Mechanics Department

Mail Code 0219 Virginia Polytechnic Institute and State University

Blacksburg, VA 24061, USA

(Received March 16, 2001)

ABSTRACT: A finite element code, in modular form, has been developed to model the complete three-dimensional resin film infusion (RFI) process. The problem formulation and its analysis incorporate compaction of the anisotropic elastic porous preform, elastic deformations of the tooling components, heat transfer in the resin, flow of resin through the preform, cure kinetics of the resin, and the heat transfer between the tools and the surrounding environment in the autoclave. The inertia effects and the transfer of heat by convection have been neglected. Two techniques, namely the slideline algorithm and a compliant layer interface, are used to model the possible sliding of the tool over the preform at their common interfaces. Weak forms are derived for (a) the initial-boundary-value problem corresponding to the transient thermal problem, (b) the boundary-value problem for the fluid through an elastic porous medium, and (c) the boundary-value problems for the quasistatic deformations of the tooling components and for a partially or fully saturated porous elastic preform. The finite element method is used to solve these equations, and the flow front is located by using a control volume technique. Computed results are presented for a stiffened *T*-panel and a two-stiffener panel.

KEY WORDS: resin film infusion, composite manufacturing, textile preform, process modeling.

INTRODUCTION

THE RESIN FILM infusion (RFI) process is a cost-effective fabrication technique for the manufacture of complex shaped composite structures [1–3]. Dry textile preforms are resin impregnated consolidated and cured in a single step thereby eliminating costly prepreg tape manufacture and ply-by-ply lay-up. Analytical and numerical methods are needed to find an optimum set of material properties and processing parameters that control the resin infiltration and cure of textile composites [1,2,4–7].

*Author to whom correspondence should be addressed. E-mail: aloos@vt.edu

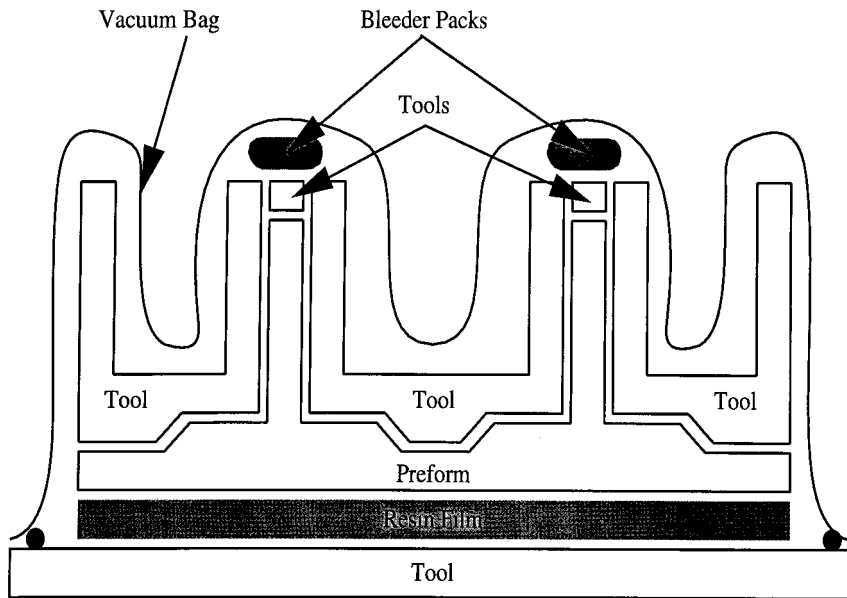


Figure 1. Schematic sketch of the components of an RFI process.

Figure 1 depicts the set-up for manufacturing a two-blade stiffened panel by the RFI method. The resin film of appropriate and not necessarily uniform thickness is placed between the base plate and dry preform. The aluminum tooling blocks and the bleeder packs are located, a vacuum bag is placed over the tool and taped to the base plate, and the entire assembly is placed in an autoclave. A predetermined temperature and pressure cycle is applied to the assembly. The heat melts the resin thus facilitating its flow into the preform, and the pressure compacts the fabric preform to the desired fiber volume fraction (FVF) and forces the resin into the preform. After the preform has been saturated with the resin, and the resin has been cured, the manufactured part is taken out of the assembly.

A finite element code has been developed to model the entire process. It computes the infiltration time and the final shape of the manufactured component.

FORMULATION OF THE PROBLEM

Governing Equations

In rectangular Cartesian coordinates, the thermomechanical deformations of the initially stress free tooling components and the partially or fully saturated preform are governed by the balance equations

$$\sigma_{ij,j} = 0, \quad (1)$$

$$\rho c_p \dot{T} = -q_{i,i} + \dot{Q}, \quad (2)$$

the constitutive relations

$$\sigma_{ij} = C_{ijkl}[e_{kl} - \alpha_{kl}(T - T_0)] - F\bar{\phi}p\delta_{ij}, \quad (3)$$

$$q_i = -k_{ij}T_{,j}, \quad (4)$$

the strain–displacement relations

$$e_{kl} = \frac{1}{2}(u_{k,l} + u_{l,k}), \quad (5)$$

the boundary conditions

$$\sigma_{ij}n_j = -Pn_i \quad \text{on } \Gamma_1, \quad (6)$$

$$u_i = 0 \quad \text{on } \Gamma_2, \quad (7)$$

$$T = \hat{T} \quad \text{on } \Gamma_3, \quad (8)$$

$$-k_{ij}T_{,j}n_i = h(T - T_\infty) \quad \text{on } \Gamma_4, \quad (9)$$

and the initial conditions

$$T(x, 0) = T_0. \quad (10)$$

Here, $\sigma_{ij} = \sigma_{ji}$ is the stress tensor, a comma followed by the index j denotes partial differentiation with respect to x_j , a superimposed dot indicates the material time derivative (here a partial derivative with respect to time t since the heat transfer due to convection has been neglected) and a repeated index implies summation over the range of the index. The effects of body and inertia forces have been neglected. Furthermore, C_{ijkl} is the elasticity matrix for the porous elastic preform, k_{ij} its thermal conductivity, ρ the mass density, c_p the specific heat, q_i the heat flux, e_{kl} the infinitesimal strain tensor, T the present temperature, T_0 the reference temperature, α_{kl} the coefficients of thermal expansion, F the volume fraction of a pore occupied by the fluid, $\bar{\phi}$ the porosity of the preform, and p the pressure exerted by the fluid. For the tooling blocks, $\bar{\phi} = 0$. Also, u_i is the displacement, P the applied pressure, n_i a unit outward normal to the boundary, Γ_1 and Γ_2 are disjoint parts of the boundary, Γ , \hat{Q} the rate of heat generation due to exothermic chemical reactions that occur during curing of the resin, \hat{T} the prescribed temperature and h the coefficient of convective heat transfer. Γ_3 and Γ_4 are disjoint parts of the boundary of the region comprising of the entire assembly. At an insulated surface, $h = 0$. The adjoining surfaces between the tool and the preform are assumed to be in contact at all times. Thus surface tractions, the temperature, and the normal component of the heat flux and of the displacement are assumed to be continuous across all interfaces; however, tangential displacements may be discontinuous to allow for the relative sliding between the contacting bodies. The dependence of the elasticities C_{ijkl} and the thermal conductivities k_{ij} upon the resin content in the preform is discussed later in this section.

The resin film is assumed to have melted at time $t = 0$, the molten resin is modeled as a homogeneous and incompressible Newtonian fluid, and its flow in a porous medium

is governed by the continuity equation and Darcy's law [8], viz.,

$$v_{i,i} = 0, \quad v_i = -\frac{S_{ij}}{\mu\phi} p_{,j}, \quad (11)$$

where v_i is the velocity of the fluid, μ its viscosity, and S_{ij} the permeability tensor. Here, the effects of inertia, body, capillary and surface tension forces have been neglected. Equations (11) are supplemented by the boundary conditions

$$p = \hat{p} \quad \text{on} \quad \Gamma_5, \quad v_i n_i = Q \quad \text{on} \quad \Gamma_6, \quad (12)$$

where \hat{p} is a prescribed pressure, Q the normal component of velocity, and Γ_5 and Γ_6 are disjoint parts of the boundary of the region occupied by the resin. At the flow front, $\hat{p} = 0$. Note that the region occupied by the resin varies with time until all the preform has been saturated with the resin. The dependence of the permeability upon the porosity is described later.

The evolution of temperature in the resin is governed by Equations (2), (4), and (8)–(10). Because of the low speed of the resin, heat transfer due to convection is neglected [4–7]. The volumetric heat transfer between the resin and the fibers due to the small difference between their temperature, though not explicitly stated in Equation (2), is accounted for in the solution of the problem by the finite element method.

Cure Kinetics of the Resin

The cure rate, $\dot{\bar{\alpha}}$, of an amine-cured epoxy resin can be described by the autocatalytic reaction [9]

$$\dot{\bar{\alpha}} = (\bar{k}_1 + \bar{k}_2 \bar{\alpha}^m) (1 - \bar{\alpha})^n, \quad (13)$$

$$\bar{k}_i = A_i \exp\left(-\frac{E_i}{RT}\right), \quad i = 1, 2, \quad (\text{no sum on } i), \quad (14)$$

where A_i is the Arrhenius pre-exponential factor, E_i the Arrhenius activation energy, R the gas constant, m a kinetic exponent, and n is the reaction order. Neglecting convection and diffusion, the degree of cure, $\bar{\alpha}$, is found by integrating Equation (13). The rate of heat generated, \dot{Q} , is assumed to be proportional to $\dot{\bar{\alpha}}$.

The resin viscosity, μ , is taken to depend upon the temperature, T , and the degree of cure, $\bar{\alpha}$, as follows:

$$\mu(T, \bar{\alpha}) = \mu_0(T) (1 - \bar{\alpha})^{A(T) + B(T)\bar{\alpha}}. \quad (15)$$

Here, μ_0 is the viscosity at $\bar{\alpha} = 0$, and A and B are temperature dependent parameters. Expression (15) for μ is similar to that given by Castro and Macosko [10].

As the resin cures, it changes from a viscous liquid to a solid. Thus, the values of the specific heat, mass density, thermal conductivity, elastic modulus, Poisson's ratio, and the

coefficient of thermal expansion depend upon the degree of cure. Since the dependence of these quantities upon $\bar{\alpha}$ is unknown, for the sake of simplicity, we assume that each one of these properties varies linearly between $\bar{\alpha}_1$ and $\bar{\alpha}_2$ [11]. That is,

$$W = \begin{cases} W_{uc}, & \bar{\alpha} \leq \bar{\alpha}_1, \\ \frac{(W_c - W_{uc})}{(\bar{\alpha}_2 - \bar{\alpha}_1)}(\bar{\alpha} - \bar{\alpha}_1), & \bar{\alpha}_1 \leq \bar{\alpha} \leq \bar{\alpha}_2, \\ W_c, & \bar{\alpha} \geq \bar{\alpha}_2, \end{cases} \quad (16)$$

where W stands for any one of the resin properties, and W_{uc} and W_c denote, respectively, the values of W in the uncured and cured states.

Dependence of Material Properties upon the Fiber Volume Fraction and the Resin Content

For an orthotropic preform, the permeability tensor S_{ij} in Equation (11) has three nonzero components when the coordinate axes are aligned along the principal material axes. Each one of the principal permeabilities, S_{11} , S_{22} , S_{33} , is assumed to depend upon the fiber volume fraction, v_f , or the porosity $\bar{\phi} = 1 - v_f$ through the relation

$$S_{ii} = a_i(1 - \bar{\phi})^{b_i}, \quad i = 1, 2, 3, \quad i \text{ not summed.}$$

Values of a_1 , b_1 , a_2 , b_2 , a_3 and b_3 are determined from the test data.

The effective or the equivalent mass density and the specific heat of a resin filled preform are computed by using the rule of mixtures, i.e.,

$$\begin{aligned} \rho &= (1 - \bar{\phi})\rho^f + \bar{\phi}F\rho^r, \\ c_p &= (1 - \bar{\phi})c_p^f + \bar{\phi}Fc_p^r, \end{aligned} \quad (17)$$

where F is the fill factor, and superscripts f and r on a quantity denote its values for the fiber and the resin, respectively. Following Chamis [12], the longitudinal and the transverse thermal conductivities (along and perpendicular to the fibers) are computed from

$$\begin{aligned} k_L &= (1 - \bar{\phi})k_L^f + \bar{\phi}Fk^r, \\ k_T &= 0.01k_T^f(1 - F) + [1 - (1 - \bar{\phi})^{1/2}]Fk^r + \frac{(1 - \bar{\phi})^{1/2}Fk^r}{1 - (1 - \bar{\phi})^{1/2}[1 - (Fk^r/k_T^r)]}, \end{aligned} \quad (18)$$

where subscripts L and T denote the longitudinal and the transverse directions, respectively. Note that for $F=0$, the transverse conductivity, k_T , has a very small value. These thermal conductivities need to be transformed to the global coordinate axes since the latter are not generally aligned along and perpendicular to the fibers. Sections of the preform are usually constructed by stacking together several layers and stitching them

through the thickness. Let fibers in layer i be oriented at an angle θ_i with the global x_1 axis. The effective conductivities of a stack of layers of the resin and the fiber are given by [13]

$$\begin{aligned}
 k_{11} &= k_L \frac{\sum_{i=1}^N h_i \cos^2 \theta_i}{\sum_{i=1}^N h_i} + k_T \frac{\sum_{i=1}^N h_i \sin^2 \theta_i}{\sum_{i=1}^N h_i}, \\
 k_{12} &= (k_L - k_T) \frac{\sum_{i=1}^N h_i \sin \theta_i \cos \theta_i}{\sum_{i=1}^N h_i}, \\
 k_{22} &= k_L \frac{\sum_{i=1}^N h_i \sin^2 \theta_i}{\sum_{i=1}^N h_i} + k_T \frac{\sum_{i=1}^N h_i \cos^2 \theta_i}{\sum_{i=1}^N h_i}, \\
 k_{33} &= k_T,
 \end{aligned}
 \tag{19}$$

where N is the number of layers and h_i is the thickness of the i th layer.

The longitudinal and the transverse coefficients of thermal expansion of a single layer of unidirectional fibers filled with resin are [12]

$$\begin{aligned}
 \alpha_L &= \frac{(1 - \bar{\phi}) \alpha_L^f E_L^f + \bar{\phi} F \alpha^r E^r}{(1 - \bar{\phi}) E_L^f + \bar{\phi} F E^r}, \\
 \alpha_T &= (1 - \bar{\phi})^{1/2} \alpha_T^f + [1 - (1 - \bar{\phi})^{1/2}] \left[1 + \frac{(1 - \bar{\phi}) F \nu^r E^r}{(1 - \bar{\phi}) E_L^f + \bar{\phi} F E^r} \right] F \alpha^r.
 \end{aligned}
 \tag{20}$$

The effective coefficients of thermal expansion for a stack of resin impregnated fibers are obtained from Equations (19) by substituting α for k . Values of Young’s moduli in the three material principal directions were computed by using relations analogous to Equations (17).

The elastic modulus of the dry preform in the thickness direction is taken to be a function of the porosity, and this functional dependence is determined from the experimental data. The value for the effective modulus of the resin can be approximated from the value of its bulk modulus. This value is much larger than the range of values for the modulus of the dry preform, so the modulus of the dry preform can be taken as a constant. The effective modulus in the thickness direction of the preform partially or completely filled with the resin is obtained from

$$E_{TT} = E_{TT}^f + F \bar{\phi} E^r
 \tag{21}$$

where the subscript TT denotes the thickness direction. The in-plane moduli are taken to equal $10E_{TT}$.

The effective Poisson’s ratios of the preform filled with the resin are assumed to be given by

$$\nu_{LA} = \nu_{LT} = \nu_{AT} = \nu^f + F \bar{\phi} \nu^r
 \tag{22}$$

where subscripts L , T and A signify, respectively, the longitudinal, the thickness and the across directions. The values of the shear moduli G_{LA} , G_{LT} and G_{AT} are computed from

$$G_{LA} = \frac{E_{TT}}{2(1 + \nu_{LA})} = G_{LT} = G_{AT}.
 \tag{23}$$

Thus, a resin filled preform is modeled as a transversely isotropic material with the axis of transverse isotropy along the thickness direction.

Equation for the Determination of the Porosity $\bar{\phi}$

The relation between the porosity $\bar{\phi}$ and the normal stress $\bar{\sigma}$ in the thickness direction, obtained from the test data, has the form

$$1 - \bar{\phi} = v_f = a_0 + a_1\bar{\sigma} + a_2\bar{\sigma}^2 + a_3\bar{\sigma}^3 + a_4\bar{\sigma}^4 \tag{24}$$

where the constants $a_i (i=0,1,2,3,4)$ are determined by the least squares method.

FINITE ELEMENT FORMULATION AND SOLUTION OF THE PROBLEM

Matrix Formulation of the Problems

We illustrate the derivation of the matrix formulation of the problem defined by Equations (1), (3), (5)–(7). Taking the inner product of Equation (1) with a continuous function ϕ_i that vanishes on Γ_2 where essential boundary conditions Equation (7) are specified and $\phi_{i,j}$ is square integrable, integrating the resulting equation over the region Ω occupied by the preform and the tools, using the divergence theorem and the natural boundary conditions Equation (6), we arrive at

$$\int_{\Gamma_1} P n_i \phi_i d\Gamma + \int_{\Omega} \sigma_{ij} \phi_{(i,j)} d\Omega = 0, \tag{25}$$

where $\phi_{(i,j)} = (\phi_{i,j} + \phi_{j,i})/2$. Substitution of the constitutive relation Equation (3) into Equation (25) results in

$$\int_{\Omega} C_{ijkl} \phi_{(i,j)} e_{kl} d\Omega = - \int_{\Gamma_1} P n_i \phi_i d\Gamma + \int_{\Omega} C_{ijkl} \phi_{(i,j)} \alpha_{kl} (T - T_0) d\Omega + \int_{\Omega} F \bar{\phi} p \phi_{i,i} d\Omega. \tag{26}$$

Let

$$u_i = \sum_{\alpha=1}^n d_{\alpha i} \psi_{\alpha}, \quad \phi_i = \sum_{\alpha=1}^n c_{\alpha i} \psi_{\alpha}, \tag{27}$$

where ψ_1, ψ_2, \dots , are the finite element basis functions defined on Ω , n equals the number of nodes in the finite element mesh, and $d_{\alpha i}$ and $c_{\alpha i}$ are respectively the values of u_i and ϕ_i at node α . Substituting from Equation (27) into Equation (26) and recalling that Equation (26) must hold for every choice of ϕ_i and hence $c_{\alpha i}$, we obtain

$$K_{\alpha\beta} d_{\beta i} = F_{\alpha i}, \quad \alpha, \beta = 1, 2, \dots, n; \quad i = 1, 2, 3, \quad \text{summed on } \beta, \tag{28}$$

where

$$\mathbf{K} = \int_{\Omega} \mathbf{B}^T \mathbf{D} \mathbf{B} d\Omega, \quad e_{kl} = B_{k\alpha} d_{\alpha l}, \quad (29)$$

$$F_{\beta i} = - \int_{\Gamma_1} P n_i \psi_{\beta} d\Gamma + \int_{\Omega} C_{ijkl} \psi_{\beta, j} \alpha_{kl} (T - T_0) d\Omega + \int_{\Omega} F \bar{\phi} p \psi_{\beta, i} d\Omega, \quad (30)$$

\mathbf{D} is the 6×6 elasticity matrix derived from C_{ijkl} by using contracted notation, \mathbf{B} is the strain–displacement matrix, \mathbf{K} the stiffness matrix and \mathbf{F} the load vector. The elements of matrix \mathbf{B} involve partial derivatives of ψ_{α} with respect of x_i . We note that in Equation (29), the integration over the region Ω can be written as the sum of the integration over each element of the finite element mesh. The essential boundary conditions Equation (7) at nodes on the part Γ_2 of the boundary are satisfied by using the penalty method. Equations (28) and (30) can be written in the matrix form as

$$\mathbf{K}d = \mathbf{F}^{\text{ext}} + \mathbf{F}^{\text{th}} + \mathbf{F}^{\text{pr}}, \quad (31)$$

where \mathbf{F}^{ext} is the nodal vector of external forces, \mathbf{F}^{th} denotes the nodal forces induced by temperature changes, and \mathbf{F}^{pr} equals the nodal forces caused by the fluid pressure in the pores of the porous preform. Similarly, the matrix formulations of the boundary-value problem defined by Equations (11) and (12), and of the initial-boundary-value problem defined by Equations (2), (4) and (8)–(10) are

$$\bar{\mathbf{K}}p = \bar{\mathbf{F}}^{\text{ext}}, \quad (32)$$

$$\mathbf{H}\dot{\mathbf{T}} + \mathbf{K}_T \mathbf{T} = \mathbf{F}^t, \quad \mathbf{T}(0) = \mathbf{T}_0. \quad (33)$$

In Equation (31) $\bar{\mathbf{K}}$ may be thought of as the stiffness matrix derived from the elasticities $S_{ij}/(\mu\bar{\phi})$, \mathbf{p} is the vector of nodal pressures and $\bar{\mathbf{F}}^{\text{ext}}$ equals the vector of nodal forces induced by the prescribed normal component of velocity in Equation (12). The matrix \mathbf{H} in Equation (33) is the heat capacity matrix, and \mathbf{K}_T may be thought of as the stiffness matrix obtained from elasticities k_{ij} . The heat rate \dot{Q} and the quantity hT_{∞} make contributions to the matrix \mathbf{F}^t . Whenever $h \neq 0$, it also contributes to the matrix \mathbf{H} .

The continuity of temperature, surface tractions, the normal component of the displacements and the normal component of the heat flux at interfaces between two adjoining bodies are incorporated in Equations (30)–(33). However, the satisfaction of the essential boundary conditions and the possible sliding of tools over the preform are to be taken care of. As stated earlier, the essential boundary conditions are satisfied by using the penalty method [14].

Contact Surfaces

The possible sliding of one body over the other at their common interface and their noninterpenetration into each other is satisfied either by using a slideline algorithm (e.g. see Hallquist et al. [15]) or using a complaint interface layer. In the slideline algorithm, one side of an interface between two contacting bodies is referred to as the master surface,

and the other the slave surface. Because of the symmetry of the approach, the choice of the slave and the master surfaces is arbitrary. Each surface is discretized independently of the other. Loosely speaking, each node is connected to the other surface by a stiff spring and a suitable force is applied to the nodes. These stiffness and forces are adjusted to prevent penetration of a node into the adjoining surface. The technique is computationally expensive in time dependent problems.

In the compliant layer method, the contacting surfaces are physically separated by a thin layer which is stiff in the thickness direction but easily deformable in shear. Thus, the compliant layer needs to be discretized, and the stiffnesses of its elements incorporated into the finite element Equations (31)–(33). The quality of the computed solution depends upon the thickness of the compliant layer, and mechanical properties assigned to its material.

Equations (31)–(33) are coupled and nonlinear because resin properties depend upon temperature and the degree of cure $\bar{\alpha}$, $\bar{\alpha}$ depends upon the temperature history, \mathbf{F}^{pr} depends upon the fluid pressure, and elasticities of the resin filled preform depend upon the porosity and the properties of the resin, etc. The backward difference method is used to solve the coupled nonlinear ordinary differential Equations (33) subject to the given initial conditions. During each time step, the material properties are assumed to be constant and equal to those evaluated at the state corresponding to the beginning of the time step. Equation (32) subject to the prescribed essential boundary conditions is solved for the pressure field p in the resin, and the velocity field is then computed from Darcy's law (11). The resin flow into each control volume is found and the location of the flow front is updated. Equation (31) is solved for the nodal displacements which help determine the compaction of the preform and also the stresses in it. The normal stress in the thickness direction is used to update the porosity at the integration points. Equation (13) is integrated at the quadrature points to find the degree of cure of the resin.

Once the preform has been filled with the resin, the flow part of the computations, i.e., the solution of Equation (32) is terminated. As soon as all of the resin has cured, the cooling of the assembly to room temperature is accomplished in one time step since the material properties remain constant in time. Surface tractions equal and opposite to those exerted by the manufactured part on the tool are applied to the manufactured part, and the final shape of the part is computed. This last step is equivalent to removing the tools from the assembly.

Flow Front Tracking

A control volume technique is used to track the moving flow front. A control volume is associated with each node in the mesh, and its shape and size depend upon the structure of the mesh. For the eight-node brick elements used herein, an element is subdivided into eight similar sub-volumes. The sub-volumes associated with a node constitute its control volume. The amount of resin flowing into each sub-volume is computed from the velocity field and the face area of its bounding surfaces. After each time step, the fill factor for the control volume is updated and the approximate location of the flow front is constructed from the nodes that have partially filled control volumes. The time step in the time marching scheme equals the minimum time required to fill a partially filled control volume. Additional details about the flow front tracking may be found in [16].

Salient Features of the Code

A finite element code capable of solving the aforesaid problem has been developed in a modular form. The options include the solution of only the flow problem, the heat transfer problem and either one or both of these in conjunction with the compaction problem. The code employs eight-noded brick elements, $2 \times 2 \times 2$ integration rule and a sparse equations solver. It computes values of permeabilities, thermal conductivities and elasticities with respect to global axes from their values given with respect to the material principal axes. The commercial program PATRAN is used to pre- and post-process the data. Both the slideline algorithm and the compliant layer model are included to account for the noninterpenetration of the two contacting bodies and the relative sliding between them. The former technique is computationally more expensive than the latter one.

COMPUTATION AND DISCUSSION OF RESULTS

Each module of the finite element code was validated as described in [6,7,17]. Here we give results for two problems. The first problem uses the geometry of a single blade stiffened preform while the second problem uses the geometry of a two-blade stiffened preform. The material properties for the skin of the preforms were taken to be those of a multiaxial warp knit (MAWK) fabric that contains seven layers of unidirectional carbon fibers (Tenax HTA) laid up in quasi-isotropic stacking sequence. The seven layers are knitted together with a polyester thread, and the knitted unit is referred to as a "stack". The stack is taken to be an orthotropic material. Details of the warp knit fabric can be found in [18–20].

The preform stiffeners are a stitched triaxial braided carbon fiber fabric. The tows are braided around a cylindrical mandrel to form a tube. The tubes were fabricated with Hexcel AS4 6k carbon fiber bias yarns at a braid angle of 60° and with IM7 36k carbon fiber axial yarns. The tube is flattened to form a layer.

To construct a preform, the stacks or tubes of material are cut to the desired dimensions and stacked together. The material is then stitched through the thickness using a modified lock stitch and Kevlar thread. The stitch rows on all materials tested were 0.51 cm part and the stitch step was 0.32 cm.

Comparison of Results Computed with a Compliant Interface Layer and a Slide Surface

The RFI process for a single stiffener panel was simulated for comparing results with the two methods of accounting for the contact conditions at an interface between two bodies. Because of the symmetry of the problem about the xy (or 12) and yz (or 23) planes passing through the centroid of the panel, only a quarter of the panel, shown in Figure 2, was studied. The preform skin was made of eight stacks of the MAWK fabric and the blade was constructed from the 14 tube braided material. In the interface layer model, 1-mm thick regions, shown shaded in Figure 2, of the 6061-T6 aluminum tool and the base plate were presumed to be made of a material very weak in shearing

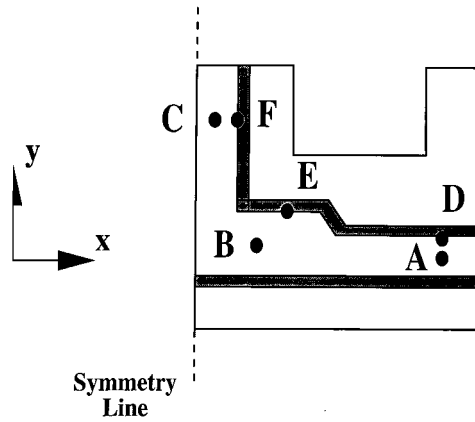


Figure 2. Schematic diagram of a one-fourth section of the single stiffener panel with interface layers and locations of sampling points A through F

deformations but stiff with respect to axial deformations. For the material of the interface layer, we took

$$E_{11} = E_{22} = E_{33} = 50 \text{ MPa}, \quad \nu_{12} = \nu_{23} = \nu_{31} = 0.33,$$

$$G_{12} = G_{23} = G_{31} = 1 \text{ kPa}, \quad \alpha_{11} = \alpha_{22} = \alpha_{33} = 1.0 \times 10^{-6} / ^\circ\text{C}.$$

In order to avoid excessive distortions of the material in the corner where the two compliant layers meet, we set $G_{12} = G_{23} = G_{31} = 10 \text{ kPa}$.

The finite element mesh for the case of the interface layer had 2396 nodes, and 1608 eight-noded brick elements, while that for the slide surface case had 2672 nodes, and 1608 eight-noded brick elements. In each case, three elements were used in the thickness or the z direction. Figure 2 also depicts the locations of points A through F where the two solutions were compared.

The autoclave pressure was assumed to vary linearly from 10 Pa at $t=0$ to 1 MPa at $t=300 \text{ s}$ and subsequently held constant at 1 MPa. The autoclave temperature increased linearly from 20°C at $t=0$ to 121°C at $t=2000 \text{ s}$, was held constant until $t=10,500 \text{ s}$, then increased at the rate of $1^\circ\text{C}/\text{min}$. to 177°C at $t=13,860 \text{ s}$ and subsequently held constant at 177°C . Values of various thermophysical parameters for the preform, aluminum tool and resin are listed in [17].

The time required to completely fill the preform, flange and the stiffener equaled 55.24 and 55.08 min. for the interface layer and the slide surface models, respectively; the corresponding times to cure the entire resin were 298.24 and 298.83 min. Thus the two models give virtually identical values of the fill and cure times. However, the CPU times with the interface model was only one-third of that with the slide surface model.

Time histories of the three normal stresses (σ_{11} , σ_{22} and σ_{33}) at point B, and of the three displacement components at point E computed with the two methods are exhibited in Figures 3 and 4, respectively; qualitatively similar results were obtained at the other four points and are given in [17]. It is clear that the two methods give virtually the same values of the normal stresses at point B; however, the displacements computed with the two methods differ somewhat. Whereas the displacements in the y - or x_2 -direction computed

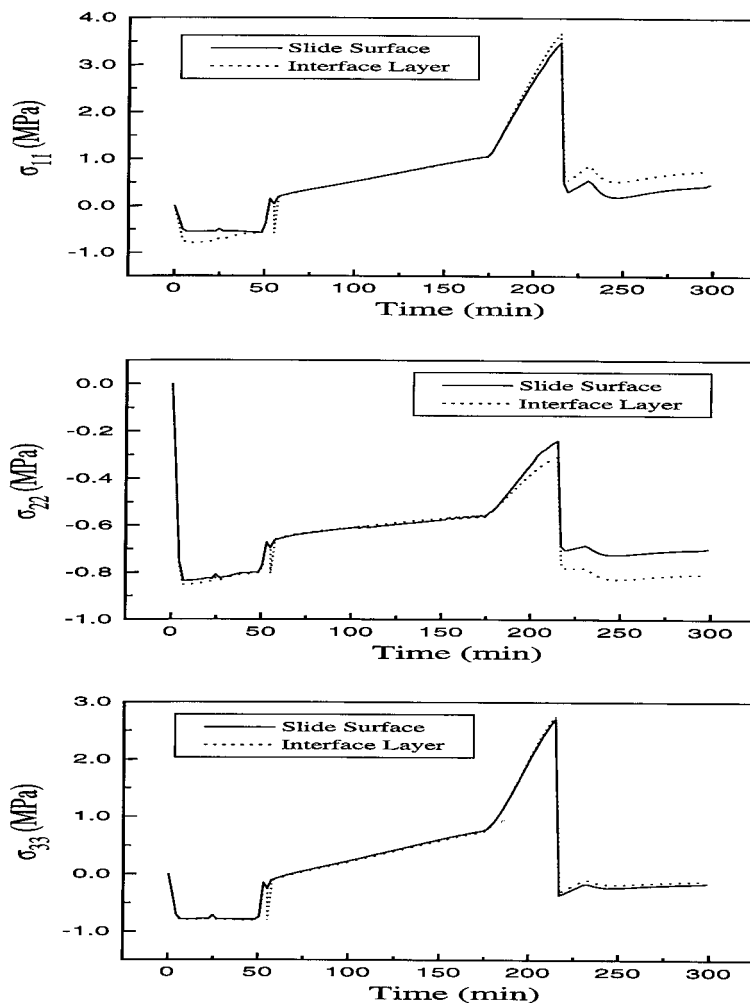


Figure 3. Time histories of normal stress components at point B.

with the two methods are essentially identical to each other, the x_3 displacement computed with the interface layer model is uniformly larger in magnitude than that obtained with the slide surface model. However, the reverse holds for the displacements in the x_1 direction. Thus both methods enforce well the non-interpenetration condition. The nonuniform distribution of the resin in the bottom part of the preform during the initial filling process causes a slight tilting of the elements. In the slide surface model, tangential forces are applied at the nodes on the interface which induce additional tangential displacements. However, in the compliant interface layer model, no such forces are applied and the small value assigned to the tangential stiffness of the complaint layer restricts the tangential displacements of the nodes. Since the time histories of stresses and displacements have been computed only until 300 min and not through the complete cool down of the part, the thickness of the cured stiffener, flange and the preform with the two methods have not been computed.

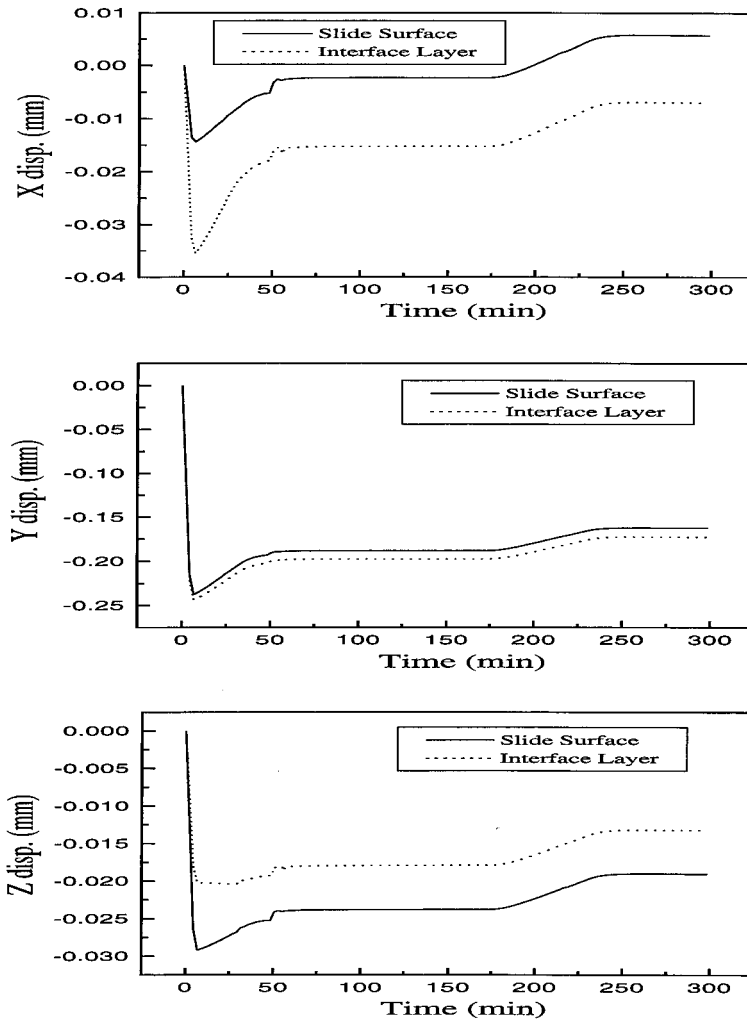


Figure 4. Time histories of displacement components at point E.

Modeling of Flow, Heat Transfer and Compaction

The finite element code was used to stimulate the manufacturing of a two stiffener panel by the RFI process. Because of the two planes of symmetry, only a quarter of the panel was analysed and the mesh is shown in Figure 5. The mesh for the analysis of the flow problem had 4832 nodes and 3870 elements, and that for the thermal and compaction problems contained 10228 nodes and 8520 elements. All of the tooling components were made of 6061-T6 aluminum, the preform skin was 8 stack MAWK Tenax, the flange was 4 tube braid, the stiffener was 14 tube braid, and the material of the complaint layer was the same as that in the example problem described above. The dimensions of the preform are shown in Figure 6 and the values of various material parameters and the autoclave cycle used are listed in [17].

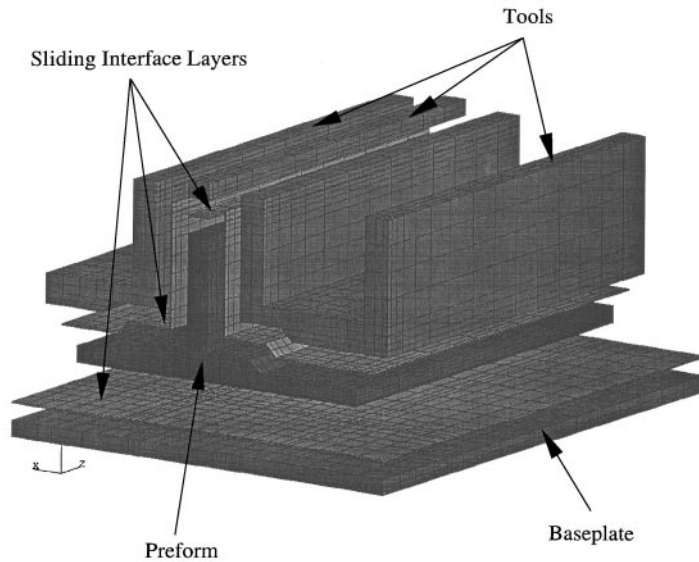


Figure 5. Magnified view of the finite element mesh.

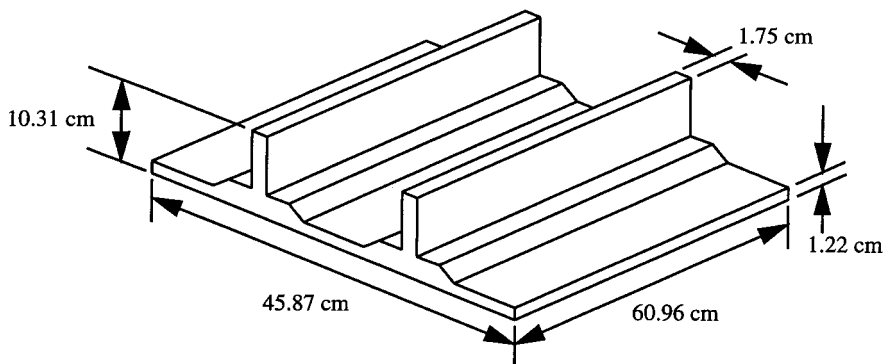


Figure 6. Sketch of the two-stiffener preform.

The thermal boundary conditions consisted of the autoclave temperatures and heat transfer coefficients. At the upper and lower surfaces, the heat transfer coefficients were set equal to $30 \text{ W/m}^2 \text{ K}$, and $25 \text{ W/m}^2 \text{ K}$, respectively. The mechanical boundary conditions consisted of symmetry boundary conditions on the two planes of symmetry, and zero tangential tractions and zero vertical displacements on the bottom surface of the base plate.

Two cases were run; the flow and heat transfer only analysis in 3DINFIL and the flow, heat transfer, and compaction options of 3DINFIL. Unless otherwise noted, the results presented in this section are for the case run with compaction.

The shape of the manufactured part at a cure time of 252 min is shown in Figure 7. An interesting result of the simulation is that the bending of the tool near the root of the stiffener causes a narrowing of the root of the stiffener. This is in qualitative agreement

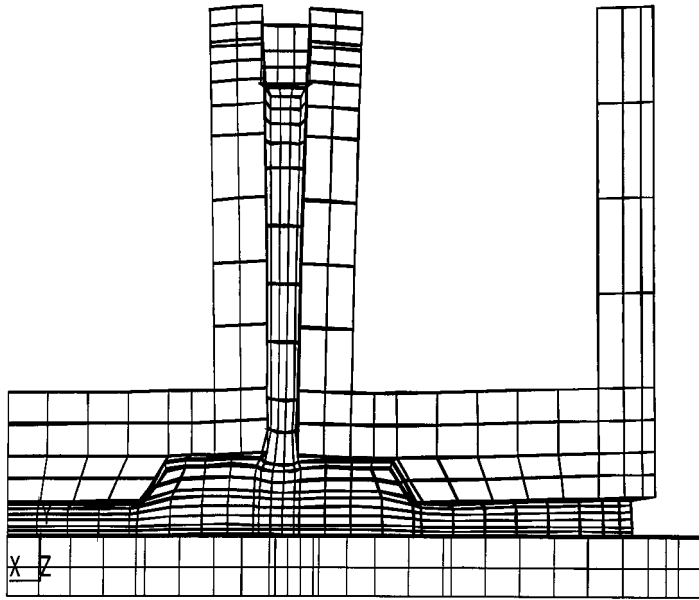


Figure 7. Shape of the manufactured part at cure (251 min); displacements have been magnified by a factor of 30.

with experimental observations. The root of the manufactured stiffener was found to be 0.33–0.66 mm narrower than the top of the stiffener.

In the analysis with compaction, the FVF at a point is updated after each time step. The FVF at the time of complete infiltration, 87.9 min, is shown in Figure 8. The empirical fits of FVF versus pressure for the skin material (MAWK Tenax, 8 stack) give a FVF of 63.8% for an applied pressure of 791kPa (115 psi). The simulated FVF at points in the skin away from the stiffener and the flange varies between 63.8 and 64.4%. At the base of the blade, the FVF is as high as 65.0% at some points. This is possibly caused by the deflection of the tool which exerted more pressure at the root of the stiffener than at the top.

Infiltration times with and without compaction analysis are shown in Figure 9. Dielectric and flush mount pressure transducer sensors [6,7,17] were mounted in the tool to measure the wet-out times at the five locations shown in the figure. All sensors at location 5 failed during the experiment. The wet-out time for sensor 1 on the top of the skin is the same for both analyses. This is to be expected because the normal stress on the skin in the compaction case is close to the autoclave pressure, and the autoclave pressure was used to calculate the FVF for the non-compaction case. At the remaining locations, the calculated wet-out times with the compaction analysis were 5–17% higher than those without the compaction. This could be due to the deflection of the tool which increased pressure and the FVF at the root of the stiffener. The resulting lower permeability decreases the flow rate and thus it takes longer for the resin to reach the top of the stiffener.

Figure 10 shows the final shape of the manufactured part after the tools have been removed. The analysis shows that the free corner of the simulated part is warped down about 0.11 mm.

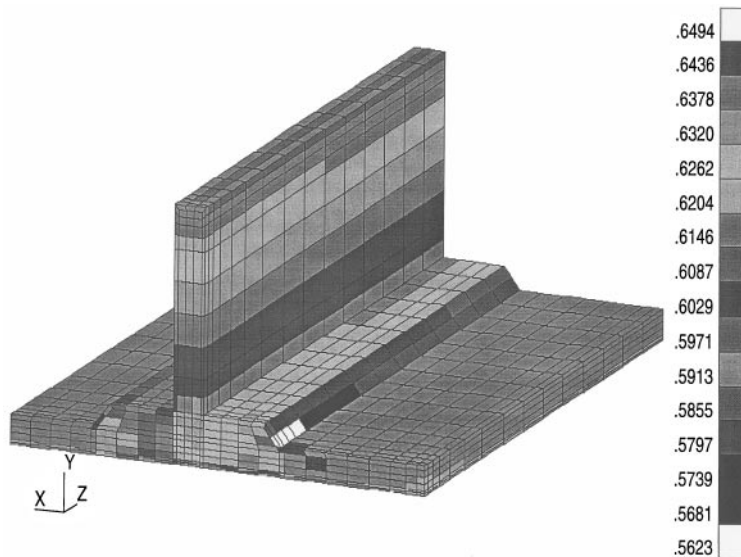


Figure 8. Fiber volume fraction distribution at the time of complete infiltration.

CONCLUSIONS

The objective of this investigation was to develop and verify a comprehensive three-dimensional model which can be used to simulate the RFI manufacturing process of complex shaped composite structures. For a specified cure cycle, the model can be used to predict the following parameters during infiltration and cure: (a) the flow front position and total infiltration time; (b) temperature distributions in the preform and tooling components; (c) the resin viscosity and degree of cure; (d) the preform deformations, fiber volume fractions and permeabilities, and (e) the final shape of the cured structure and the residual stress distribution.

The model formulation includes submodels that describe preform compaction, resin flow, heat transfer, resin cure kinetics, and residual stresses. The compaction problem is coupled with the fluid flow and heat transfer problems through the pressure and temperature terms in the constitutive relation. The resin cure kinetics mode is used to predict the cure rate, degree of cure, and resin viscosity required for solution of the heat transfer and resin flow problems.

The governing equations are solved numerically by the finite element technique. A three-dimensional finite element computer code, 3DINFIL was written. The code uses eight-noded brick elements, and the eight-point Gaussian integration rule. A direct sparse solver is used to solve the set of linear algebraic equations that result from the finite element discretization. The code has a database of material models that contain values of various material parameters needed for each analysis.

Material properties are required to solve the equations for the flow, heat transfer and compaction problems. Some of the properties were experimentally determined, and others were obtained from the literature. The properties of the resin saturated and unsaturated regions of the preform were determined by a rule of mixtures from the properties of the resin and the preform.

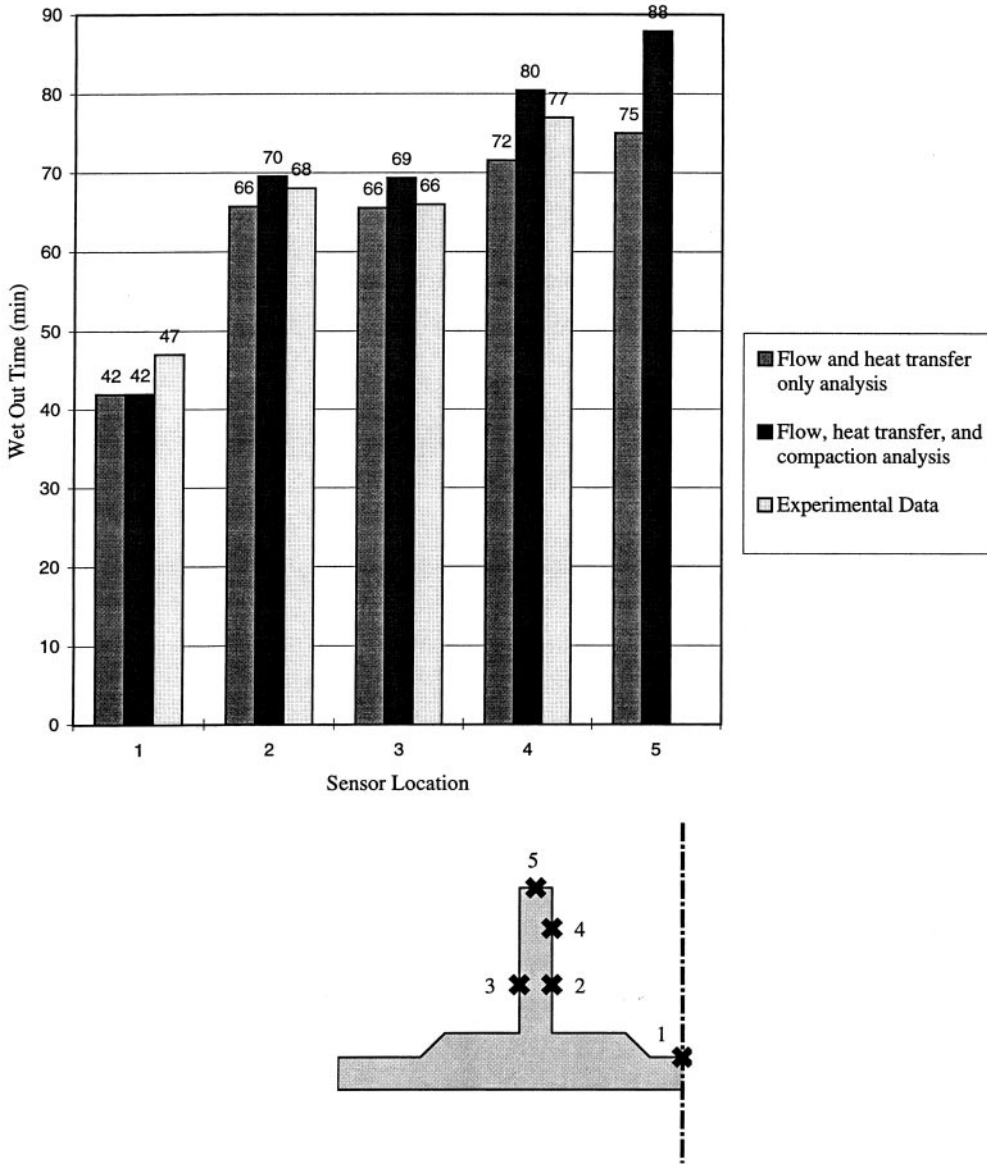


Figure 9. Predicted and measured infiltration times at five different locations in the preform.

A slide surface algorithm was developed to accurately compute the deformations during the RFI process. During processing, adjacent bodies may slide with respect to each other on the common interface. The algorithm couples the two adjoining bodies and allows for their independent sliding and deformation. However, since the algorithm is computationally expensive, a compliant interface model was developed. In this approach, a thin layer is introduced between two contacting bodies. The layer is stiff in the thickness direction but can be easily deformed in shear. The quality of the computer solution depends on the thickness and the stiffness of the compliant layer.

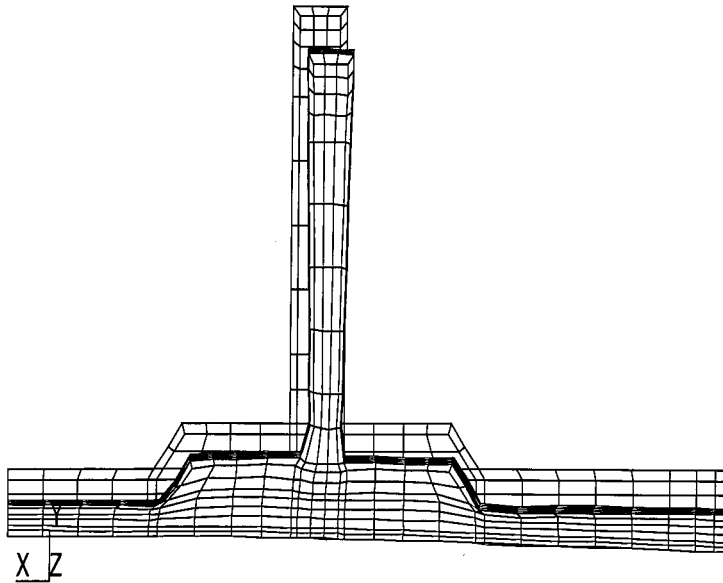


Figure 10. Final warpage of the preform after the tool removal. The final configuration has been overlaid on the undeformed shape, and displacements have been magnified by a factor of 30.

A model with interface layers, and a model with slide surfaces were created to compare the solutions of the two methods. The RFI process for a single stiffener panel was simulated for this study. From the study, it can be concluded that the interface layer model is a good practical alternative to the slide surface model. The interface layer model requires only one-third of the CPU time needed for the slide surface model, and gives at critical points normal stresses close to those computed with the slide surface model.

The manufacture of a two-stiffener panel by the RFI process was simulated by 3DINFIL with and without the compaction option. For the case without compaction, the calculated infiltration times were within 20% of the measure values. The calculated wet-out times with the compaction analysis were 5–17% higher than those without compaction most likely due to a decrease in preform permeability caused by the tool deflection.

ACKNOWLEDGMENT

This work was supported by NASA Langley Research Center, grant NASI-1881 and by the Boeing Company, Long Beach, CA, under contract NASI-20546.

REFERENCES

1. Weideman, M.H., Loos, A.C., Dexter, H.B. and Hasko, G.H. (1992). An infiltration/cure model for manufacture of fabric composites by the resin infusion process. Report no. CCMS 92-05, Virginia Tech Center for Composite Materials and Structures.
2. Ahn, K.J., Seferis, J.C. and Letterman, L. (1990). Autoclave resin infusion process: analysis and prediction of resin content. *SAMPE Quart.*, **21**: 3–10.

3. Chen, V., Hawley, A., Klotzsche, M., Markus, A. and Palmer, R. (1991). Composite technology for transport primary structure. *1st NASA Advanced Composite Technology Conference*, NASA Conf. Publ. 3104, Part 1, pp. 71–126.
4. Loos, A.C. and MacRae, J.D. (1996). A process simulation model for manufacture of a blade stiffened panel by the resin film infusion process. *Composites Science and Technology*, **56**: 273–289.
5. Loos, A.C., MacRae, J.D., Hood, D., Kranbuehl, D.E. and Dexter, H.B. (1996). Resin film infusion (RFI) process simulation of complex shaped composite structures. In: *Proceedings of the 37th AIAA/ASME/ASCE/AHS/ASC Structures, Structural Dynamics and Materials Conference*. Salt Lake City, UT, April 15–17. Paper No. AIAA-96-1533-CP, AIAA, Reston, VA. pp. 1828–1837.
6. Caba, A.C., Loos, A.C., Rattazzi, D. and Batra, R.C. (1998). A three-dimensional simulation model of the resin film infusion manufacturing process. In: *Proceedings of the 30th International SAMPE Technical Conference*. pp. 329–340.
7. Caba, A.C., Rattazzi, D., Batra, R. and Loos, A.C. (1999). Verification of a simulation model of resin film infusion of a stiffened panel. *Journal of Reinforced Plastics and Composites*, **18**(16): 1465–1478.
8. Davé, R. (1991). A unified approach to modeling resin flow during composite processing. *Journal of Composite Materials*, **24**: 22–41.
9. Dutta, A. and Ryan, M.E. (1979). Effect of fillers on kinetics of epoxy cure. *Journal of Applied Polymer Science*, **24**: 635–649.
10. Castro, J.M. and Macosko, C.W. (1982). Studies of mold filling and curing in the reaction injection molding process. *AIChE Journal*, **28**(2): 250–260.
11. White, S.R. and Hahn, H.T. (1992). Process modeling of composite materials: residual stress development during cure. Part II, experimental validation. *Journal of Composite Materials*, **26**: 2423–2453.
12. Chamis, C. (1983). Simplified composite micromechanics equations for hygral, thermal and mechanical properties. In: *38th Annual Conference*. The Society of Plastics Industry, Session 21C: pp. 1–9.
13. Shen, C.H. and Springer, G.S. (1976). Moisture absorption and desorption of composite materials. *Journal of Composite Materials*, **10**: 2–20.
14. Zienkiewicz, O.C. and Taylor, R.L. (1989). The finite element method, Fourth edn. Vol. 1. *Basic Formulation and Linear Problems*. McGraw-Hill.
15. Hallquist, J.O., Goudreau, G.L. and Benson, D.J. (1985). Sliding interfaces with contact-impact in large-scale lagrangian computations. *Computer Methods in Applied Mechanics and Engineering*, **51**: 107–137.
16. Fracchia, C.A., Castro, J. and Tucker, C.L. (1989). A finite element/control volume simulation of resin transfer molding filling. In: *Proceedings of the American Society for Composites*. Fourth Technical Conference. pp. 157–166.
17. Loos, A.C., Batra, R.C., Rattazzi, D., Caba, A.C. and Knott, T. (1999). Process model development/residual stress model development. Final Report prepared for the Boeing Company, Long Beach, CA.
18. Dexter, H.B., Palmer, R.J. and Hasko, G.H. (June 7–11 1993). Mechanical properties and damage tolerance of multiaxial warp knit structural elements. In: *Fourth NASA/DOD Advanced Composites Technology Conference*, NASA CP-3229.
19. Hinrichs, S., Palmer, R.J., Ghumman, A., Deaton, J., Furrow, K.W. and Dickinson, L.C. (1994). Mechanical property evaluation of stitched/rfi composites. In: *Fifth NASA/DOD Advanced Composites Technology Conference*, NASA CP-3294. August 22–25.
20. Furrow, K.W. (April 1996). Material property evaluation of braided and braided/woven wing skin blade stiffeners. Contractor Report 198303, NASA.